

Bottleneck-Free Hot Hole Cooling in CH₃NH₃PbI₃ Revealed by Femtosecond XUV Absorption.

Max Verkamp¹, Joshua Leveille², Aastha Sharma¹, André Schleife^{2,3,4}, and Josh Vura-Weis^{1}*

¹ Department of Chemistry, University of Illinois at Urbana-Champaign, Urbana, IL

² Department of Materials Science and Engineering, University of Illinois at Urbana-Champaign, Urbana, IL

³ Materials Research Laboratory, University of Illinois at Urbana-Champaign, Urbana, IL

⁴ National Center for Supercomputing Applications, University of Illinois at Urbana-Champaign, Urbana, IL

Abstract

Femtosecond carrier cooling in the organohalide perovskite semiconductor CH₃NH₃PbI₃ is measured using extreme ultraviolet (XUV) and optical transient absorption spectroscopy. XUV absorption between 44 eV and 58 eV measures transitions from the I 4*d* core to the valence and conduction bands and gives distinct signals for hole and electron dynamics. The core-to-valence-band signal directly maps the photoexcited hole distribution and provides a quantitative measurement of the hole temperature. The combination of XUV and optical probes reveals that upon excitation at 400 nm, the initial hole distribution is 3.5 times hotter than the electron distribution. At an initial carrier density of $1.4 \times 10^{20} \text{ cm}^{-3}$ both carriers are subject to a hot phonon bottleneck, but at $4.2 \times 10^{19} \text{ cm}^{-3}$ the holes cool to less than 1000 K within 400 fs. This result places significant constraints on the use of organohalide perovskites in hot-carrier photovoltaics.

Introduction

Lead halide perovskites such as CH₃NH₃PbI₃ show significant promise for use in next generation photovoltaics¹⁻⁴ and other opto-electronic applications.⁵⁻⁷ Underlying their success is a direct band gap that can be synthetically tuned for optimal performance and simple solution-based fabrication. One of the most transformative possibilities envisioned for these semiconductors is their use in hot-carrier solar cells.^{8,9} Traditional photovoltaics are limited to a maximum theoretical efficiency of 34% due in part to rapid carrier cooling: while a semiconductor with a small band gap can absorb most of the solar spectrum,

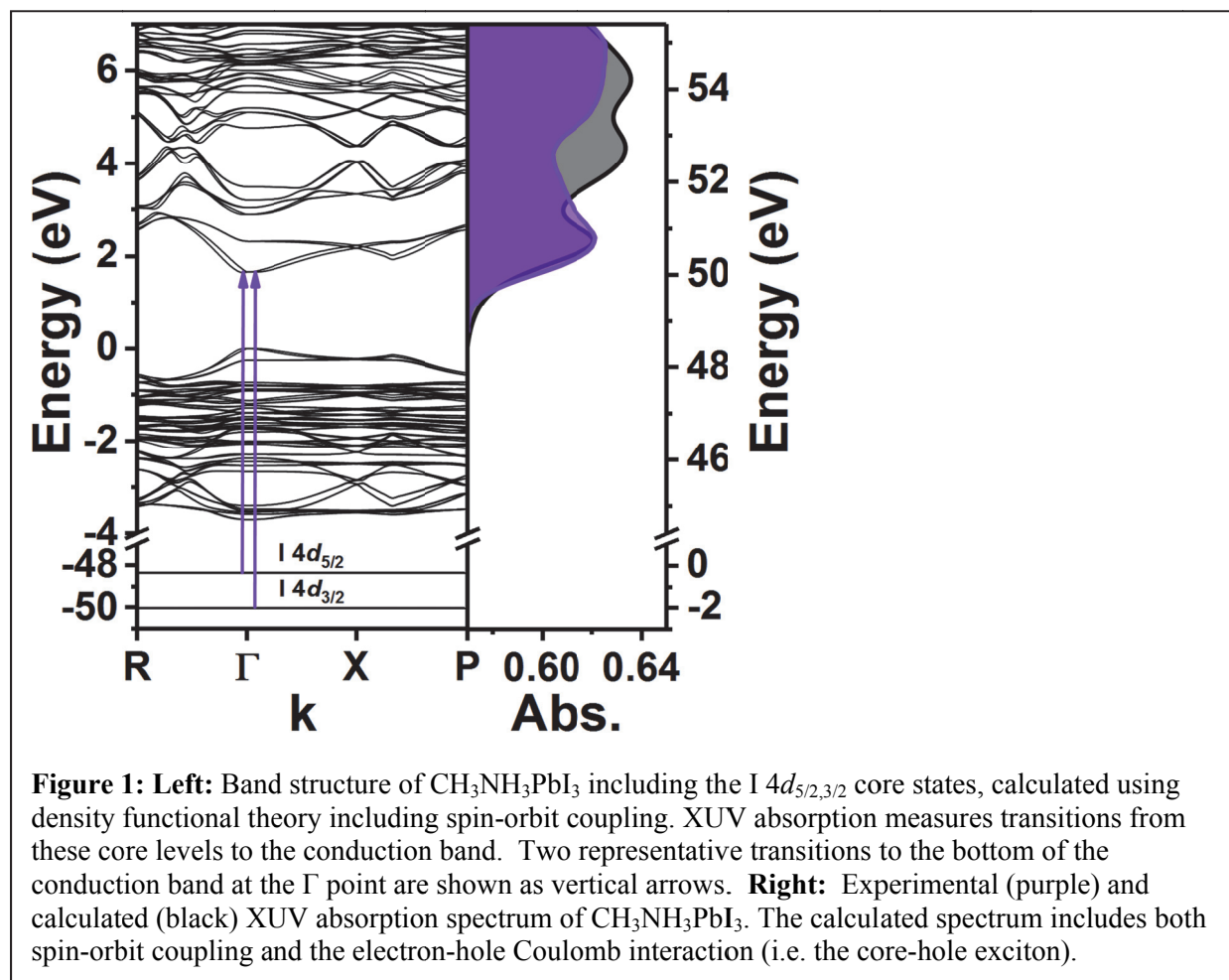
the excess energy of short-wavelength photons is rapidly lost to heat. If this transfer of energy from the carriers to the lattice is slow, hot carriers can be collected at higher voltages. Such devices could be up to 66% efficient,¹⁰ almost doubling the standard performance limit.

A series of reports show intriguingly slow carrier cooling rates in lead halide perovskites above a photoinduced carrier density of $\sim 10^{18} \text{ cm}^{-3}$. Optical transient absorption spectroscopy, which reports on the joint distribution of the electrons and holes, revealed cooling times of ~ 10 ps.¹¹⁻¹⁴ Two-photon photoemission directly measures the energy distribution of electrons in the conduction band, and was used to observe a population of hot electrons that lasted for ~ 100 ps.¹⁵ Time-resolved ARPES can measure photoexcited hole distributions¹⁶ but has not yet been applied to these materials. It is therefore unclear whether the holes cool slowly and are amenable to hot-carrier collection. While hot electron and hole transfer to molecular layers has been reported at femtosecond timescales,^{17,18} perovskite photovoltaics that take advantage of the hot phonon bottleneck have not been reported.

In this work, we use transient extreme ultraviolet (XUV) spectroscopy and optical transient absorption to reveal that the initial distribution of energy between the electrons and holes is unequal and that they cool to the band edges at different rates. While optical transient absorption measures transitions from the valence band to the conduction band, XUV transient absorption measures transitions from atomic core levels to the conduction band and to valence band holes. The XUV probe therefore provides unique spectroscopic signatures for the photoexcited electrons and holes, and has been used to measure carrier relaxation in semiconductors such as Si, Ge, and PbI_2 at femtosecond to attosecond timescales.¹⁹⁻²² By combining the two probes, we quantitatively measure the distinct temperature and cooling mechanism of each carrier and show that holes begin with an average energy 3.5 times higher than the electrons. However, they cool rapidly to the band edge and are not subject to a hot phonon bottleneck until very high carrier density.

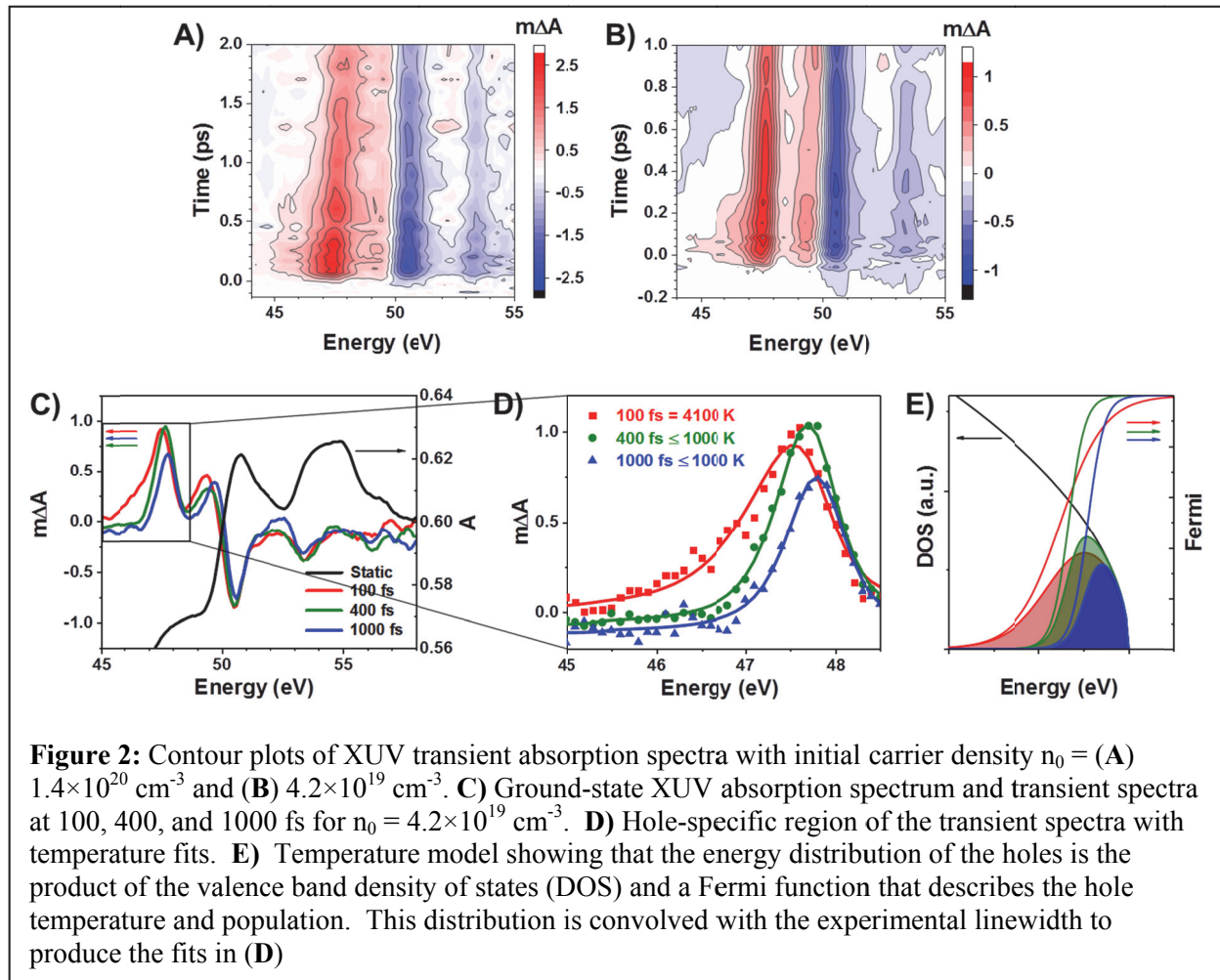
Results

Thin films (~ 70 nm) of $\text{CH}_3\text{NH}_3\text{PbI}_3$ were prepared by thermal evaporation of PbI_2 followed by vapor annealing in $\text{CH}_3\text{NH}_3\text{I}$. Figure 1 shows the band structure including the I $4d_{5/2}$ and $4d_{3/2}$ core levels as calculated using density functional theory, along with the experimental and computed ground-state XUV absorption spectra. As we and others have recently shown,^{20,21,23} the XUV spectrum measures the unoccupied density of states convolved with the core-hole spin-orbit splitting and contributions from the core-hole exciton.



The sample was photoexcited at 400 nm and probed using an XUV continuum produced using high-harmonic generation with a tabletop, laser-based source with a time resolution of 100 fs FWHM.²¹ Contour plots of the resulting transient absorption spectrum $[\Delta A = -\log_{10}(I_{\text{pump-on}}/I_{\text{pump-off}})]$ are

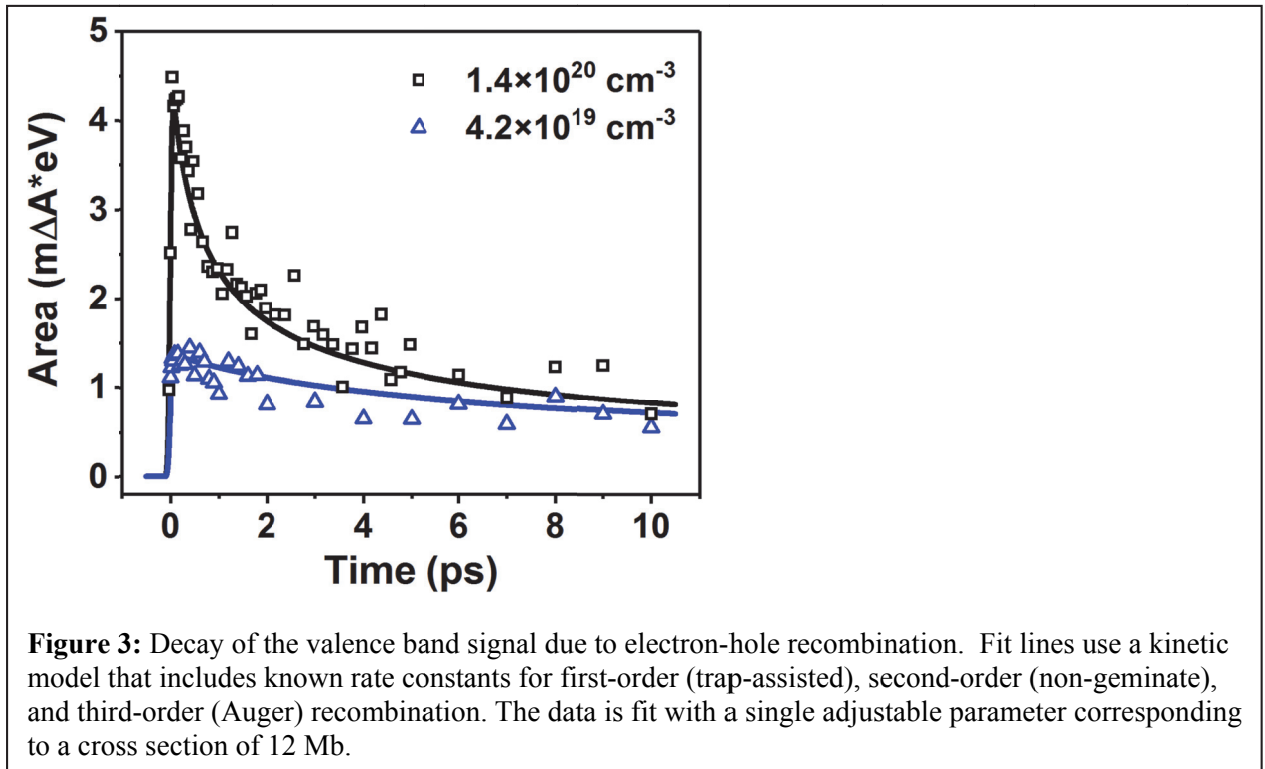
shown in Figure 2A and 2B for two different initial carrier concentrations, $n_0 = 1.4 \times 10^{20} \text{ cm}^{-3}$ and $n_0 = 4.2 \times 10^{19} \text{ cm}^{-3}$. The ground state absorption spectrum and slices of the transient spectrum at 100 fs, 400 fs, and 1000 fs for the low-power data set are shown in Figure 2C. As we recently showed for PbI_2 ,²¹ transient features below the onset of the ground-state absorption at 49.1 eV are caused by transitions from the $I 4d_{5/2}$ core to the photoinduced valence band (VB) hole. Band-gap renormalization and band-filling in the conduction band (CB) modify the $I 4d_{3/2,5/2} \rightarrow \text{CB}$ absorption, leading to the features from 48.8 to 55.0 eV. The positive feature at 49.3 eV also includes the $I 4d_{3/2} \rightarrow \text{VB}$ contribution, which is blueshifted by the 1.7 eV core-hole spin-orbit splitting from the $I 4d_{5/2} \rightarrow \text{VB}$ feature at 47.6 eV. Because of the comparative simplicity of the valence band signal, this work focuses on interpretation of the hole dynamics, with a discussion of the conduction band dynamics given in the Supporting Information.



In both the high-power and low-power experiments (Figure 2A and 2B), the hole signal from 45.0 to 48.5 eV narrows and decays over time. Figure 2D zooms in on this feature for the low-power data set. At 100 fs after photoexcitation the signal is broad and asymmetric, with a tail at low energy that extends below 46 eV. By 400 fs, the spectrum has narrowed and sharpened to a symmetric Voigt lineshape. Between 400 fs and 1000 fs, this spectrum decreases in height and blueshifts by 0.1 eV. These spectra are analyzed using the straightforward model in Figure 2E, in which the energy distribution of the hole is the product of the valence band density of states (modeled as a parabolic band¹²⁻¹⁴) and a Fermi function that describes the hole temperature and population. The electrons and holes each achieve well-defined thermal distributions within 80 fs after excitation,¹¹ and can thereafter each be described with a Fermi temperature. The XUV absorption spectrum is the convolution of this distribution with the Gaussian spectrometer resolution of 0.5 eV and Lorentzian core-hole lifetime broadening of 0.45 eV. The area of the peak measures the population of holes, while the asymmetry measures their temperature. Given the experimental signal-to-noise and peak broadening, temperatures as low as 1000 K can be measured.

While this model fits the spectra well and is intuitively appealing, it is not obvious that there should be a 1:1 correspondence between the strength of the absorption and the hole population. For example, there could be a larger transition dipole moment for the core-to-VB transition at the band edge compared to deep in the band, as was recently observed in XUV transient absorption of Si.²⁰ We show that such effects in $\text{CH}_3\text{NH}_3\text{PbI}_3$ are minimal by measuring the area of the hole feature as a function of time for two pump fluences, and comparing the resulting dynamics to known carrier recombination rates (Figure 3).²⁴ At an initial carrier density of $1.4 \times 10^{20} \text{ cm}^{-3}$, the area drops by half in 2 ps due to Auger recombination, followed by a slow decay on the tens-of-ps timescale. With $4.2 \times 10^{19} \text{ cm}^{-3}$ initial carriers, only the slow decay component is observed. Carrier recombination in $\text{CH}_3\text{NH}_3\text{PbI}_3$ proceeds via first-order (trap-assisted), second-order (non-geminate), and third-order (Auger) pathways, and rate constants for each pathway have been previously measured using optical transient absorption.¹³ Using those reported rate constants and the known initial carrier densities, both the high- and low-power XUV data sets are simultaneously fit using a single adjustable parameter, namely the absorption cross section per

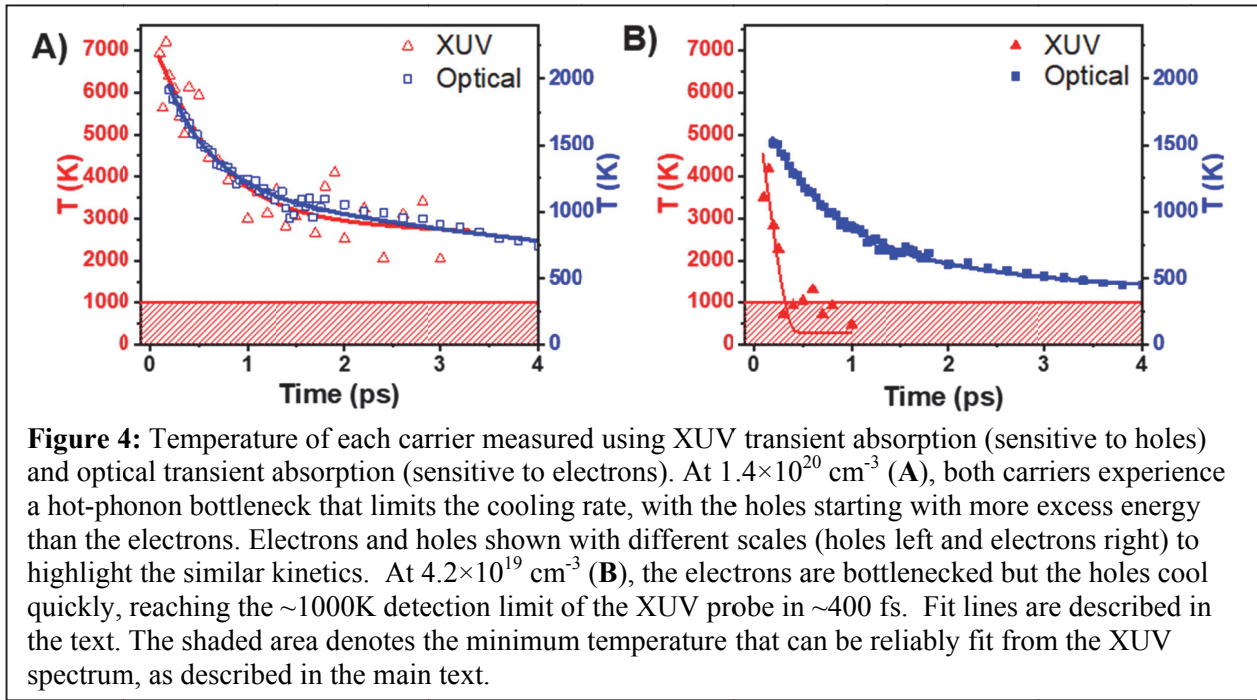
hole. The fitted value of $3.2 \times 10^{-23} \text{ eV} \cdot \Delta A \cdot \text{cm}^3$ corresponds to a cross section of 12 Mb, and it is a good match for the DFT-predicted value of 16 Mb. Given the excellent match between the measured area of the hole signal and the decay predicted by the known recombination rate constants, we conclude that any energy dependence of the absorption strength is weak in this system and can be ignored in the temperature analysis that follows (i.e. we can treat the $I 4d_{5/2} \rightarrow \text{VB}$ transition dipole matrix element as a constant and focus on the density of states and Fermi occupation).



Previous optical transient absorption studies of $\text{CH}_3\text{NH}_3\text{PbI}_3$ have measured the carrier temperature using an analysis similar to that shown in Figure 2E. The two carriers can in principle have different temperatures, due to k-point dependence of the initial photoexcitation and/or different carrier cooling rates. In semiconductors such as GaAs in which electrons and holes have very different effective masses, optical transient absorption selectively measures the temperature of the lighter carrier. For $\text{CH}_3\text{NH}_3\text{PbI}_3$, however, the electron ($m_e^* = 0.23m_0$) is only slightly lighter than the hole ($m_h^* = 0.29m_0$).²⁵ As shown in the Supporting Information, optical transient absorption in this case primarily measures the

colder carrier temperature with a slight inherent preference for the electron due to the effective mass difference. XUV transient absorption, on the other hand, provides a distinct spectroscopic measurement of the hole temperature. The combination of optical and XUV probes can therefore measure the temperatures of each carrier as they cool to the band edge.

Figure 4 shows the temperature measured using each technique as a function of time for two initial carrier concentrations, $1.4 \times 10^{20} \text{ cm}^{-3}$ and $4.2 \times 10^{19} \text{ cm}^{-3}$. For the high-power experiment (Figure 4A), the optically-measured temperature cools from $\sim 2000\text{K}$ at 200 fs to 750K at 4 ps, with approximately 40% of the initial temperature lost in the first picosecond and slower cooling from 1-4 ps. This cooling curve is consistent with that commonly observed in the perovskite literature above a critical carrier density of 10^{18} cm^{-3} ,¹²⁻¹⁴ and corresponds to the hot-phonon bottleneck regime. In this regime, the hot carriers rapidly equilibrate with a longitudinal optical phonon, and further carrier cooling is limited by coupling between that phonon and the lattice (via either acoustic or transverse optical daughter phonons).^{12-14,26} The hole-specific cooling curve measured using XUV transient absorption follows the same general shape but the absolute temperatures are 3.5 times higher, cooling from 7000K at 100 fs to



3000K at 3 ps. Given this independent measurement of the hole temperature, the optically-measured temperature is assigned to the electron. At a carrier density of $1.4 \times 10^{20} \text{ cm}^{-3}$, therefore, holes are significantly hotter than electrons but both carriers are subject to a hot-phonon bottleneck and cool slowly. As discussed in the Supporting Information, the cooling curves can be fit to give LO phonon lifetimes of $0.5 \pm 0.1 \text{ ps}$ for the XUV probe and $0.6 \pm 0.3 \text{ ps}$ for the optical probe. These time constants are in good agreement with the lifetime of 0.6 ps measured using optical transient absorption by Fu *et al.*¹²

At an initial carrier density of $4.2 \times 10^{19} \text{ cm}^{-3}$, however, the cooling behavior measured by the two techniques are drastically different (Figure 4B). The optically-measured temperature follows a similar slow cooling curve as the high-power data in Figure 4A, and gives an LO phonon lifetime of $0.8 \pm 0.2 \text{ ps}$. However, the XUV-measured hole temperature drops from 4500K to the 1000K detection limit in less than 400 fs. This rapid cooling is not consistent with a hot-phonon bottleneck, indicating that the electrons and holes must cool via distinct carrier-phonon interactions. The hole cooling is therefore fit using a Fröhlich carrier-phonon scattering model that depends on the hole-phonon scattering time τ_{h-LO} and a characteristic LO frequency ω_{LO} :

$$\frac{dT_h}{dt} = -\frac{2}{3k_B} \frac{h\omega_{LO}}{\tau_{h-LO}} \left[\exp\left(\frac{-h\omega_{LO}}{k_B T_h}\right) - \exp\left(\frac{-h\omega_{LO}}{k_B T_L}\right) \right] \quad (1)$$

T_h is the hole temperature, T_L is the lattice temperature, and k_B is the Boltzmann constant. Previous optical transient absorption spectroscopy at a wavelength sensitive to both electrons and holes using sub-10 fs pulses identified two phonon frequencies of $14 \pm 1 \text{ meV}$ and $29 \pm 2 \text{ meV}$ that were coupled to carrier relaxation,²⁷ and nonadiabatic molecular dynamics calculations found that hot holes couple preferentially phonons in the 25-40 meV range.²⁸ Using the phonon frequency of 29 meV, the characteristic hole-phonon scattering time τ_{h-LO} is fit as $8.0 \pm 2.7 \text{ fs}$. As discussed in the Supporting Information, this is consistent with the predicted effective scattering rate of 8.5 fs calculated for carrier-dipole interactions in a polar semiconductor.

Discussion

Two major conclusions are apparent from the combination of XUV and optical transient absorption spectroscopy presented above. First, the initial temperature of the holes is significantly hotter than that of the electrons. This preference for hot holes was predicted in one of the first optical transient absorption studies of $\text{CH}_3\text{NH}_3\text{PbI}_3$, which proposed that photoexcitation below 480 nm induces absorption from deep in the valence band to the conduction band edge.¹ This prediction was later supported theoretically by band-resolved optical constant analysis²⁹ and by DFT calculations of the valence and conduction band density of states in conjunction with non-adiabatic quantum dynamics.³⁰ Other theoretical treatments have predicted roughly equal initial carrier temperatures, with the primary contribution to the absorption spectrum coming from transitions between the highest valence band and the lowest conduction band along the R to M branch.^{31–33} By selectively measuring the hole temperature using XUV transient absorption, we experimentally and quantitatively confirm the hot-hole, cold-electron predictions. We note that for this asymmetric temperature distribution to persist over time the holes must be screened from the electrons, presumably by polaron formation.^{34–37} This screening is consistent with the long recombination times observed in these materials.³⁸ This result also resolves an enduring puzzle in the published carrier temperatures, in which the reported carrier temperature is not consistent with the excess energy from above-bandgap excitation. $\text{CH}_3\text{NH}_3\text{PbI}_3$ has a band gap of 1.65 eV, so photoexcitation at 400 nm (3.1 eV) should leave a total of 1.45 eV of excess energy between the electrons and holes. Many optical transient absorption experiments report initial temperatures of ~ 2000 K after 400 nm excitation,^{12–14} and frequently report this number as an average carrier temperature. Under the simplifying assumption of parabolic bands, this gives an average excess energy per carrier of 0.3 eV for a total of 0.6 eV, far below the expected value. The current measurement using the combination of XUV and optical probes gives average excess energies of 0.9 eV for the holes and 0.3 eV for the electrons. This adds up to a total of 1.2 eV, very close to the expected total of 1.45 eV. Rapid carrier cooling within the 100 fs instrument response (before onset of the hot-phonon bottleneck) accounts for the final missing 0.25 eV.

The second major conclusion from this work is that hole cooling can still be explained within the Fröhlich regime for carrier densities as high as $4.2 \times 10^{19} \text{ cm}^{-3}$, significantly higher than the 10^{18} cm^{-3} hot-phonon bottleneck threshold commonly reported using optical transient absorption spectroscopy.¹²⁻¹⁴ As discussed above, optical transient absorption preferentially measures the colder carrier (in this case the electron), so the 10^{18} cm^{-3} threshold is now shown to be specific to the electron. This difference between the electrons and holes can only be explained if the two carriers couple to different phonons, likely due to the difference in composition between the valence and conduction band. The conduction band is primarily derived from Pb $6p$ atomic orbitals, while the valence band has its greatest contribution from I $5p$. Photoexcitation therefore distributes positive charge on the Pb sublattice and negative charge on the I sublattice, producing a non-uniform charge distribution and causing a unique phonon response for each carrier. This difference has been observed experimentally in $\text{CH}_3\text{NH}_3\text{PbBr}_3$, in which transient hard x-ray spectroscopy showed that photoexcited electrons are delocalized between several Pb atoms but holes were likely localized on a single Br.³⁹ A range of computational work supports this difference in delocalization, predicting the electron polaron to be larger than the hole polaron.^{35,37} The difference in size can be connected to the onset of the hot phonon bottleneck, which has been proposed to stem from spatial overlap of polarons above a critical carrier density.³⁵ A simple space-filling model argues that this onset occurs at 10^{18} cm^{-3} for electrons in $\text{CH}_3\text{NH}_3\text{PbI}_3$, matching the optically-measured threshold. In the present work, we show that holes do not bottleneck until above 10^{19} cm^{-3} . This threshold requires the hole polarons to be at least 50% smaller than the electron polarons. The charge localization for holes and electrons was recently predicted to be spatially distinct with the hole polaron being ~30% smaller than that of the electron.³⁷ A simple model for the polaron size⁴⁰ incorporating the difference in effective masses and the difference in phonon energy observed here also predicts the hole polaron to be ~30% smaller. These are consistent with the higher threshold for the hot-phonon bottleneck observed experimentally in the present work.

From a device optimization perspective, these results impose strict limits on the use of $\text{CH}_3\text{NH}_3\text{PbI}_3$ in hot-carrier photovoltaics. This class of materials has been widely proposed as a candidate

for such devices due to the low threshold for the hot-phonon bottleneck as measured by transient optical and photoelectron spectroscopy. The results above show that not only do holes cool quickly even at high carrier concentrations, but $\sim 3/4$ of the initial excess energy from above-bandgap excitation is in the hot holes. At any reasonable light intensity, only $\sim 1/4$ of the excess energy is deposited into the slow-cooling hot electrons, severely limiting the efficiency gains possible from collecting hot carriers.

Synthetic modification of the perovskite structure may be able to reduce the negative properties found here and increase hot-carrier collection efficiency. High-harmonic sources are rapidly evolving, and the emergence of high repetition-rate, few-fs instruments will soon allow transient XUV spectroscopy to be performed at low carrier density. Combined with ultrafast optical and photoelectron probes and advances in theory, this will enable the carrier-specific cooling and phonon coupling to be measured, predicted, and potentially controlled.

Acknowledgements

The transient XUV instrument, including the nonlinear optical parametric amplifier, was built with partial funding from the Air Force Office of Scientific Research under AFOSR Awards No. FA9550-14-1-0314 and FA9550-18-1-0293. M.V. acknowledges support from the Springborn Endowment. XRD and SEM measurements were carried out in the Materials Research Laboratory (MRL) at the University of Illinois at Urbana-Champaign. Density functional theory results are based upon work supported by the National Science Foundation under Grant No. DMR-1555153. This research is part of the Blue Waters sustained-petascale computing project, which is supported by the National Science Foundation (awards OCI-0725070 and ACI-1238993) and the state of Illinois. Blue Waters is a joint effort of the University of Illinois at Urbana-Champaign and its National Center for Supercomputing Applications. We are grateful to Dr. Juergen Furthmueller for generating the I pseudopotential used in this work.

Materials and Methods

Spectroscopy

XUV transient absorption was performed using an instrument that has been previously described in detail.²¹ Briefly, the 800 nm output of a 6 mJ, 35 fs, 1 kHz titanium:sapphire amplifier is split into probe and pump paths. 4 mJ is used to drive high-harmonic generation (HHG) to generate an XUV continuum with spectral coverage from 35 to 60 eV and < 35 fs pulses. The remaining 2 mJ is used as a visible pump by doubling to 400 nm (3.1 eV) and attenuating with neutral density filters to achieve the 4.2×10^{19} and $1.4 \times 10^{20} \text{ cm}^{-3}$ excitation densities. HHG is performed in a semi-infinite gas-cell geometry using 50 Torr of argon gas as the generation medium. Absorption was measured in transmission geometry with dispersed detection onto an array CCD. Sample heating by the pump laser is minimized by flowing nitrogen gas over the samples and raster scanning the 2x2mm active area during data collection.

Computation

Density functional theory (DFT) calculations are performed using the VASP^{41,42} code using the PBE generalized-gradient approximation⁴³ to describe exchange and correlation, and the PAW method to describe the electron-ion interaction.⁴⁴ The calculated band gap is shifted to the experimental value of 1.65 eV. The complex and frequency-dependent dielectric function is calculated via solution of the Bethe-Salpeter equation (BSE) using the implementation in refs^{45,46}. This accounts for the electron-hole Coulomb attraction (i.e. core-hole exciton formation) upon XUV absorption. Electronic state energies from which the BSE is solved are obtained from density functional theory calculations, including spin-orbit coupling. Further details are given in the Supporting Information.

Sample Preparation

Methylammonium lead iodide perovskite (MAPbI₃) samples were prepared by thermal evaporation of lead iodide (Sigma Aldrich, 99%) onto 50 nm thick Si₃N₄ membranes, followed by conversion to MAPbI₃ via heating the samples under vacuum in the presence of methylammonium iodide (Sigma Aldrich, 98%) powder at 155° C for 2.5 hours. Sample characterization via x-ray diffraction, scanning electron microscopy, and visible absorption is described in the Supporting Information.

References

1. Xing, G. *et al.* Long-range balanced electron- and hole-transport lengths in organic-inorganic $\text{CH}_3\text{NH}_3\text{PbI}_3$. *Science* **342**, 344–347 (2013).
2. Grätzel, M. The light and shade of perovskite solar cells. *Nat. Mater.* **13**, 838–842 (2014).
3. Egger, D. A. *et al.* What remains unexplained about the properties of halide perovskites? *Adv. Mater.* **30**, 1800691 (2018).
4. Herz, L. M. Charge-Carrier Mobilities in Metal Halide Perovskites: Fundamental Mechanisms and Limits. *ACS Energy Lett.* **2**, 1539–1548 (2017).
5. Johnston, M. B. Optoelectronics: Colour-selective photodiodes. *Nature Photonics* **9**, 634–636 (2015).
6. Sutherland, B. R. & Sargent, E. H. Perovskite photonic sources. *Nature Photonics* **10**, 295–302 (2016).
7. Rashid, A., Mohd, B., Gao, P. & Khaja, M. Recent progress in organohalide lead perovskites for photovoltaic and optoelectronic applications. *Coord. Chem. Rev.* **373**, 258–294 (2018).
8. Kahmann, S. & Loi, M. A. Hot carrier solar cells and the potential of perovskites for breaking the Shockley-Queisser limit. *Journal of Materials Chemistry C* **7**, 2471–2486 (2019).
9. Li, M., Fu, J., Xu, Q. & Sum, T. C. Slow Hot-Carrier Cooling in Halide Perovskites: Prospects for Hot-Carrier Solar Cells. *Advanced Materials* **1802486**, 1–17 (2018).
10. Ross, R. T. & Nozik, A. J. Efficiency of Hot-Carrier Solar-Energy Converters. *J. Appl. Phys.* **53**, 3813–3818 (1982).
11. Richter, J. M. *et al.* Ultrafast carrier thermalization in lead iodide perovskite probed with two-dimensional electronic spectroscopy. *Nat. Commun.* **8**, 376 (2017).
12. Fu, J. *et al.* Hot carrier cooling mechanisms in halide perovskites. *Nat. Commun.* **8**, 1300 (2017).
13. Yang, Y. *et al.* Observation of a hot-phonon bottleneck in lead-iodide perovskites. *Nat. Photonics* **10**, 53–59 (2016).
14. Yang, J. *et al.* Acoustic-optical phonon up-conversion and hot-phonon bottleneck in lead-halide

- perovskites. *Nat. Commun.* **8**, 14120 (2017).
15. Niesner, D. *et al.* Persistent Energetic Electrons in Methylammonium Lead Iodide Perovskite Thin Films. *J. Am. Chem. Soc.* **138**, 15717–15726 (2016).
 16. Liu, F., Ziffer, M., Hansen, K. R., Wang, J. & Zhu, X. Direct Determination of Band Gap Renormalization in Photo-Excited Monolayer MoS₂. (2019).
 17. Brauer, J. C., Lee, Y. H., Nazeeruddin, M. K. & Banerji, N. Ultrafast charge carrier dynamics in CH₃NH₃PbI₃ : evidence for hot hole injection into spiro-OMeTAD. *J. Mater. Chem. C* **4**, 5922–5931 (2016).
 18. Li, M. *et al.* Slow cooling and highly efficient extraction of hot carriers in colloidal perovskite nanocrystals. *Nat. Commun.* **8**, 14350 (2017).
 19. Zürich, M. *et al.* Ultrafast carrier thermalization and trapping in silicon-germanium alloy probed by extreme ultraviolet transient absorption spectroscopy. *Struct. Dyn.* **4**, 044029 (2017).
 20. Cushing, S. K. *et al.* Hot phonon and carrier relaxation in Si(100) determined by transient extreme ultraviolet spectroscopy. *Struct. Dyn.* **5**, 054302 (2018).
 21. Lin, M.-F. *et al.* Carrier-Specific Femtosecond XUV Transient Absorption of PbI₂ Reveals Ultrafast Nonradiative Recombination. *J. Phys. Chem. C* **121**, 27886–27893 (2017).
 22. Schultze, M. *et al.* Attosecond band-gap dynamics in silicon. *Science* **346**, 1348–1352 (2014).
 23. Zürich, M. *et al.* Direct and simultaneous observation of ultrafast electron and hole dynamics in germanium. *Nat. Commun.* **8**, 15734 (2017).
 24. Sum, T. C. & Mathews, N. Advancements in Perovskite Solar Cells: Photophysics behind the Photovoltaics. *Energy Environ. Sci.* (2014).
 25. Giorgi, G., Fujisawa, J. I., Segawa, H. & Yamashita, K. Small photocarrier effective masses featuring ambipolar transport in methylammonium lead iodide perovskite: A density functional analysis. *J. Phys. Chem. Lett.* **4**, 4213–4216 (2013).
 26. Pötz, W. & Kocevar, P. Electronic power transfer in pulsed laser excitation of polar semiconductors. *Phys. Rev. B* **28**, 7040–7047 (1983).

27. Ghosh, T., Aharon, S., Etgar, L. & Ruhman, S. Free Carrier Emergence and Onset of Electron–Phonon Coupling in Methylammonium Lead Halide Perovskite Films. *J. Am. Chem. Soc.* **139**, 18262–18270 (2017).
28. Li, W., Zhou, L., Prezhd, O. V. & Akimov, A. V. Spin–Orbit Interactions Greatly Accelerate Nonradiative Dynamics in Lead Halide Perovskites. *ACS Energy Lett.* **3**, 2159–2166 (2018).
29. Chen, H. A., Lee, M. H. & Chen, C. W. Wavelength-dependent optical transition mechanisms for light-harvesting of perovskite MAPbI₃ solar cells using first-principles calculations. *J. Mater. Chem. C* **4**, 5248–5254 (2016).
30. Hedley, G. J. *et al.* Hot-Hole Cooling Controls the Initial Ultrafast Relaxation in Methylammonium Lead Iodide Perovskite. *Sci. Rep.* **8**, 1–9 (2018).
31. Even, J., Pedesseau, L. & Katan, C. Theoretical insights into multibandgap hybrid perovskites for photovoltaic applications. *SPIE Photonics Eur.* **9140**, 91400Y (2014).
32. Even, J. *et al.* Solid-state physics perspective on hybrid perovskite semiconductors. *J. Phys. Chem. C* **119**, 10161–10177 (2015).
33. Leguy, A. *et al.* Experimental and theoretical optical properties of methylammonium lead halide perovskites. *Nanoscale* **8**, 6317–6327 (2016).
34. Neukirch, A. J. *et al.* Polaron stabilization by cooperative lattice distortion and cation rotations in hybrid perovskite materials. *Nano Lett.* (2016).
35. Frost, J. M., Whalley, L. D. & Walsh, A. Slow Cooling of Hot Polarons in Halide Perovskite Solar Cells. *ACS Energy Lett.* **2**, 2647–2652 (2017).
36. Zhu, H. *et al.* Screening in crystalline liquids protects energetic carriers in hybrid perovskites. *Science* **353**, 1409–1413 (2016).
37. Miyata, K. *et al.* Large polarons in lead halide perovskites. *Sci. Adv.* **3**, e1701217 (2017).
38. Wehrenfennig, C., Eperon, G. E., Johnston, M. B., Snaith, H. J. & Herz, L. M. High Charge Carrier Mobilities and Lifetimes in Organolead Trihalide Perovskites. *Adv. Mater.* **26**, 1584–1589 (2014).

39. Santomauro, F. G. *et al.* Localized holes and delocalized electrons in photoexcited inorganic perovskites: Watching each atomic actor by picosecond X-ray absorption spectroscopy. *Struct. Dyn.* **4**, 44002 (2017).
40. Schultz, T. D. Polar Crystals: Self-Energy, Mass, and Mobility. *Phys. Rev.* **116**, 526–543 (1959).
41. Kresse, G. & Furthmüller, J. Efficient iterative schemes for ab initio total-energy calculations using a plane-wave basis set. *Phys. Rev. B* **54**, 11169–11186 (1996).
42. Kresse, G. & Joubert, D. From ultrasoft pseudopotentials to the projector augmented-wave method. *Phys. Rev. B* **59**, 1758–1775 (1999).
43. Perdew, J. P., Burke, K. & Ernzerhof, M. Generalized Gradient Approximation Made Simple. *Phys. Rev. Lett.* **77**, 3865–3868 (1996).
44. Blöchl, P. E. Projector augmented-wave method. *Phys. Rev. B* **50**, 17953–17979 (1994).
45. Rödl, C., Fuchs, F., Furthmüller, J. & Bechstedt, F. Ab initio theory of excitons and optical properties for spin-polarized systems: Application to antiferromagnetic MnO. *Phys. Rev. B* **77**, 184408 (2008).
46. Fuchs, F., Schleife, A. & Bechstedt, F. Efficient $O(n^2)$ approach to solve the Bethe-Salpeter equation for excitonic bound states. *Phys. Rev. B* **78**, 085103 (2008).

Supporting Information for
**Bottleneck-Free Hot Hole Cooling in CH₃NH₃PbI₃ Revealed by
Femtosecond XUV Absorption.**

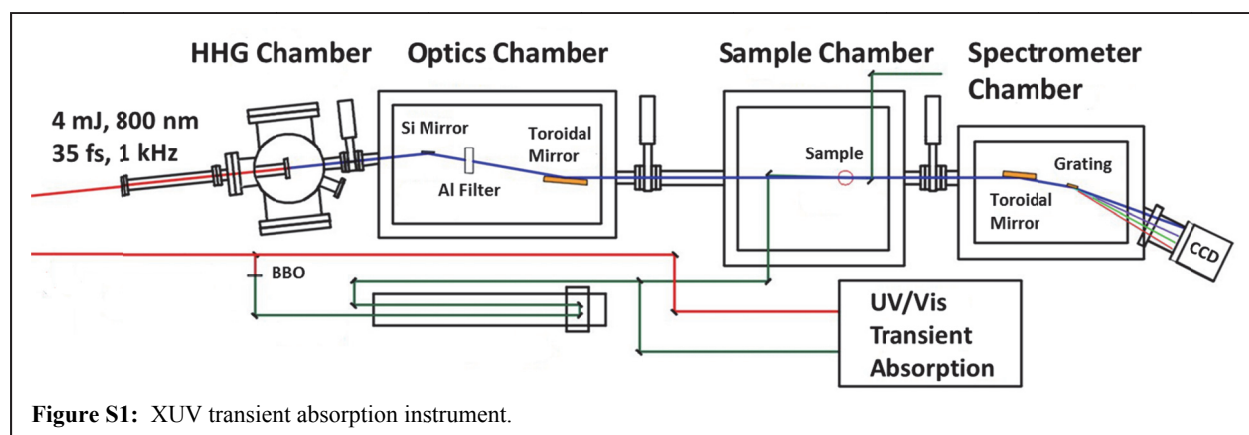
Max Verkamp¹, Joshua Leveillee², Aastha Sharma¹, André Schleife^{2,3,4}, and Josh Vura-Weis^{1}*

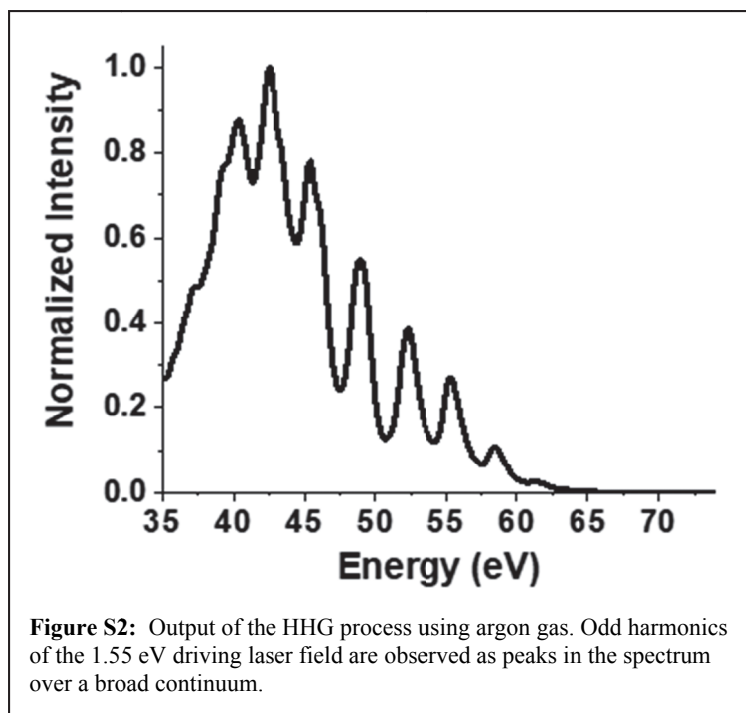
Table of Contents

1. Instrumental Methods	S2
2. Sample Preparation	S3
3. Sample Characterization	S3
4. Carrier Density Calculations	S5
5. Recombination Model Details	S6
6. Heat Baseline Correction	S7
7. Single Energy Kinetics	S8
8. Optical Transient Absorption Fitting Details	S9
9. XUV Fitting Details	S11
10. I 4d XPS to Identify the Lifetime Broadening	S12
11. Temperature vs Time Fitting Details	S13
12. Computational Details	S15
13. References	S17

1. Instrumental Methods

This work was performed using a home-built extreme ultraviolet (XUV) spectrometer, shown in Figure S1. Briefly, the 800 nm output of a 6 mJ, 35 fs, 1 kHz titanium sapphire amplifier is split to use 4 mJ to drive high-harmonic generation (HHG) to generate XUV radiation with < 35 fs pulses. The remaining 2 mJ is used as a visible pump by doubling to 400 nm (3.1 eV) and attenuating to achieve the 4.2×10^{19} and $1.4 \times 10^{20} \text{ cm}^{-3}$ excitation densities. HHG is performed in a semi-infinite gas-cell geometry using 50 Torr of argon gas as the generation medium. This gives a broad continuum, shown in Figure S2, with photons up to $\sim 60 \text{ eV}$. The driving laser is filtered out using reflection from a silicon mirror at Brewster's angle and reflection by an aluminum filter (100 nm thick). XUV light is absorbed by oxygen and nitrogen, so the system is kept at ultra-high vacuum ($< 10^{-6}$ Torr). The XUV beam is focused through the sample and then dispersed onto an array CCD for collection using toroidal optics at glancing incidence to minimize attenuation. Absorption measurements are taken in transmission geometry and transient signals are measured as change in absorption between pump-on and pump-off absorption measurements, with the delay controlled by a one-meter stage. The instrument response function was measured to be $\sim 100 \text{ fs}$, with the dominant contribution being from the pump pulse and drift between different data sets. The instrument resolution was measured to be 0.5 eV (Gaussian FWHM) using the peaks of xenon ion (ionized with the residual driving beam of the HHG process). Samples are deposited (details below) on 2 mm x 2 mm x 50 nm silicon nitride membranes. For transient measurements, the samples are raster scanned and gas cooled (using nitrogen gas) to prevent pump-induced sample damage. Several stages of differential pumping are used to reduce the impact of using a nitrogen gas flow in the ultra-high vacuum chambers.





Optical transient absorption (OTA) measurements are also performed using the same driving laser. The probe is a white light continuum generated by focusing the 800 nm pulse through a sapphire crystal. The pump is the same doubled fundamental as the XUV instrument. Absorption is measured in transmission geometry using a commercial spectrometer (Ocean Optics USB2000+) for detection and a chopper for gating between pump-on and pump-off measurements. Samples for OTA are prepared as described below on glass microscope slides.

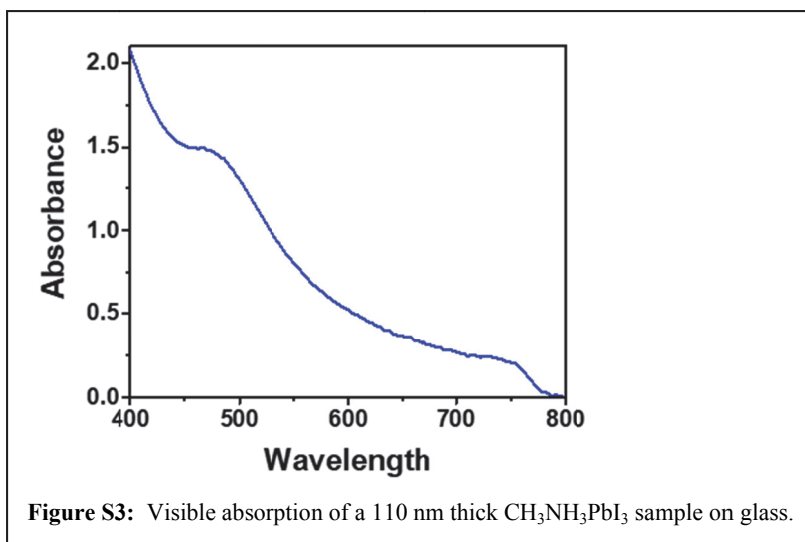
2. Sample Preparation

Methylammonium lead iodide perovskite ($\text{CH}_3\text{NH}_3\text{PbI}_3$) samples were deposited on silicon nitride membranes using gas phase techniques. First, the lead iodide is deposited on the substrate using thermal evaporation via a partially home built system (Plasmonic Technologies, LLC model LTK350-sys). The lead iodide is converted to $\text{CH}_3\text{NH}_3\text{PbI}_3$ via vapor conversion by heating the samples under vacuum in the presence of methylammonium iodide powder at 155°C for 2.5 hours.

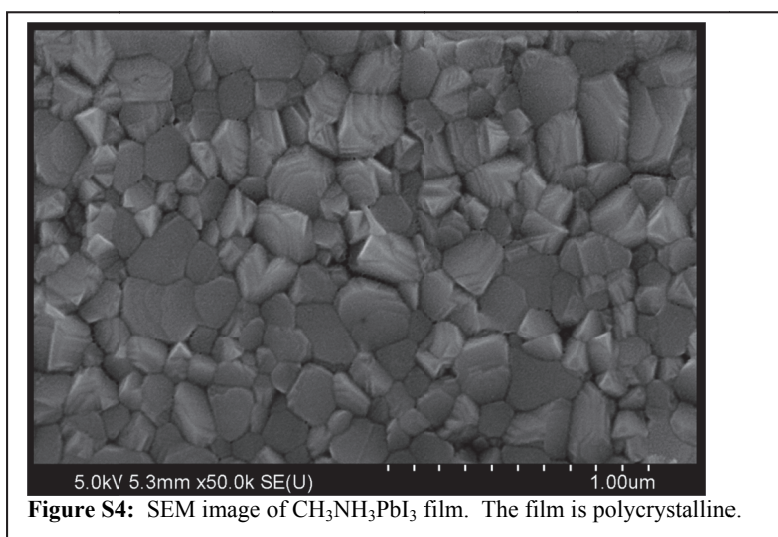
3. Sample Characterization

The samples were characterized using visible absorption, scanning electron microscopy (SEM) measured using a Hitachi S4800 High Resolution instrument, and x-ray diffraction (XRD) measured using a Panalytical/Philips X'pert 2 instrument at the Cu K- α line.

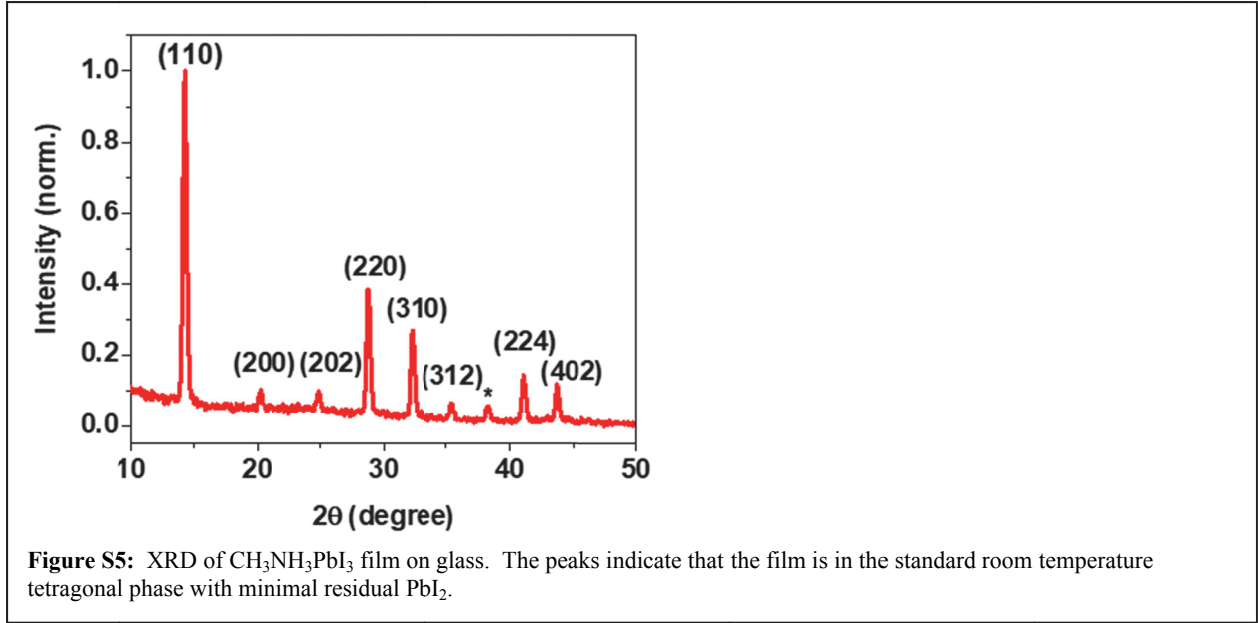
Visible absorption (Figure S3) shows the characteristic semiconductor absorption of $\text{CH}_3\text{NH}_3\text{PbI}_3$ with the band gap at 760 nm (1.65 eV). Absorption at 400 nm is used to verify the thickness of samples.



SEM (Figure S4) shows the microscopic structure of the material. The film is polycrystalline with grain sizes on the order of microns.



XRD (Figure S5) identifies the phase of perovskite present. The peak positions and intensities present are consistent with the room temperature tetragonal phase of $\text{CH}_3\text{NH}_3\text{PbI}_3$. The peak at $\sim 39^\circ$ (starred) is the (003) peak of residual PbI_2 .



4. Carrier Density Calculations

The number of photons absorbed in the full width at half maximum (FWHM) of the pump beam was calculated using the measured reflection (R) and transmission (T) of the sample and used to determine the carrier density along with the sample's penetration depth (t). The sample's thickness is approximately the penetration depth for the pump wavelength used, so an average carrier density from the total volume assuming the thickness is equal to the penetration depth is an acceptable approximation.

$$n = \frac{1 - R - T}{2 \times \pi \times \left(\frac{FWHM}{2}\right)^2 \times t} \times \frac{E_{pulse}}{\hbar\omega_{pump}}$$

n is the carrier density, E_{pulse} is the amount of energy per pump pulse, and $\hbar\omega_{pump}$ is the energy of the pump photons. The factor of 2 in the denominator comes from only 50% of the power being within the area of the FWHM.

The pump spot used was 220 μm FWHM and the probe was 65 μm FWHM. The two data sets were pumped with 0.55 μJ (high) and 0.20 μJ (low) per pulse.

5. Recombination Model Details

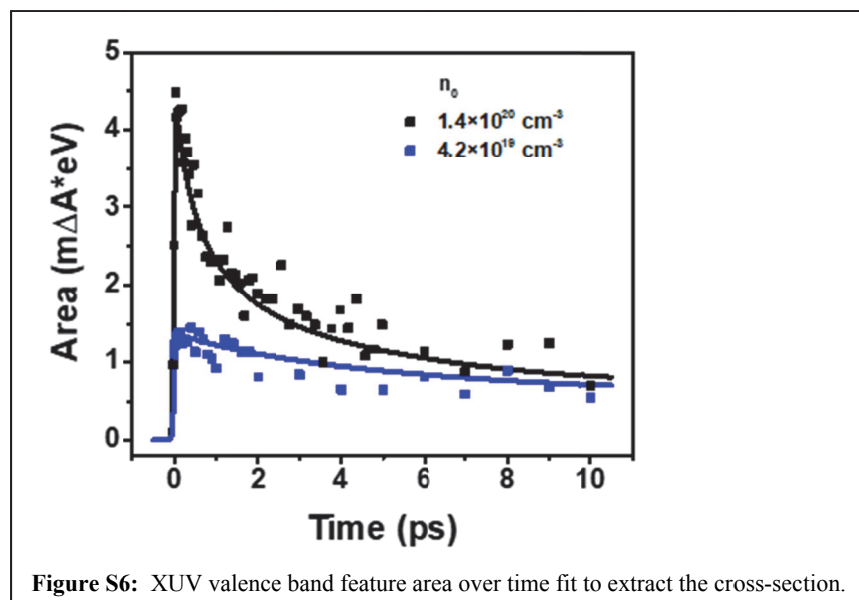
A standard three-order recombination model was used with measured initial carrier densities and literature rate constants¹ ($k_1 = 8.6 \times 10^7 \text{ s}^{-1}$, $k_2 = 9.8 \times 10^{-11} \text{ cm}^3 \cdot \text{s}^{-1}$, and $k_3 = 6.8 \times 10^{-29} \text{ cm}^6 \cdot \text{s}^{-1}$) to fit the valence band feature area over time, shown in Figure S6, to extract the cross-section.

$$-\frac{dn}{dt} = k_1 \times n + k_2 \times n^2 + k_3 \times n^3$$

n is the carrier density, t is time, and k_1 , k_2 , and k_3 are the first-, second-, and third-order recombination rate constants. The absorbance is given by Beer's law as:

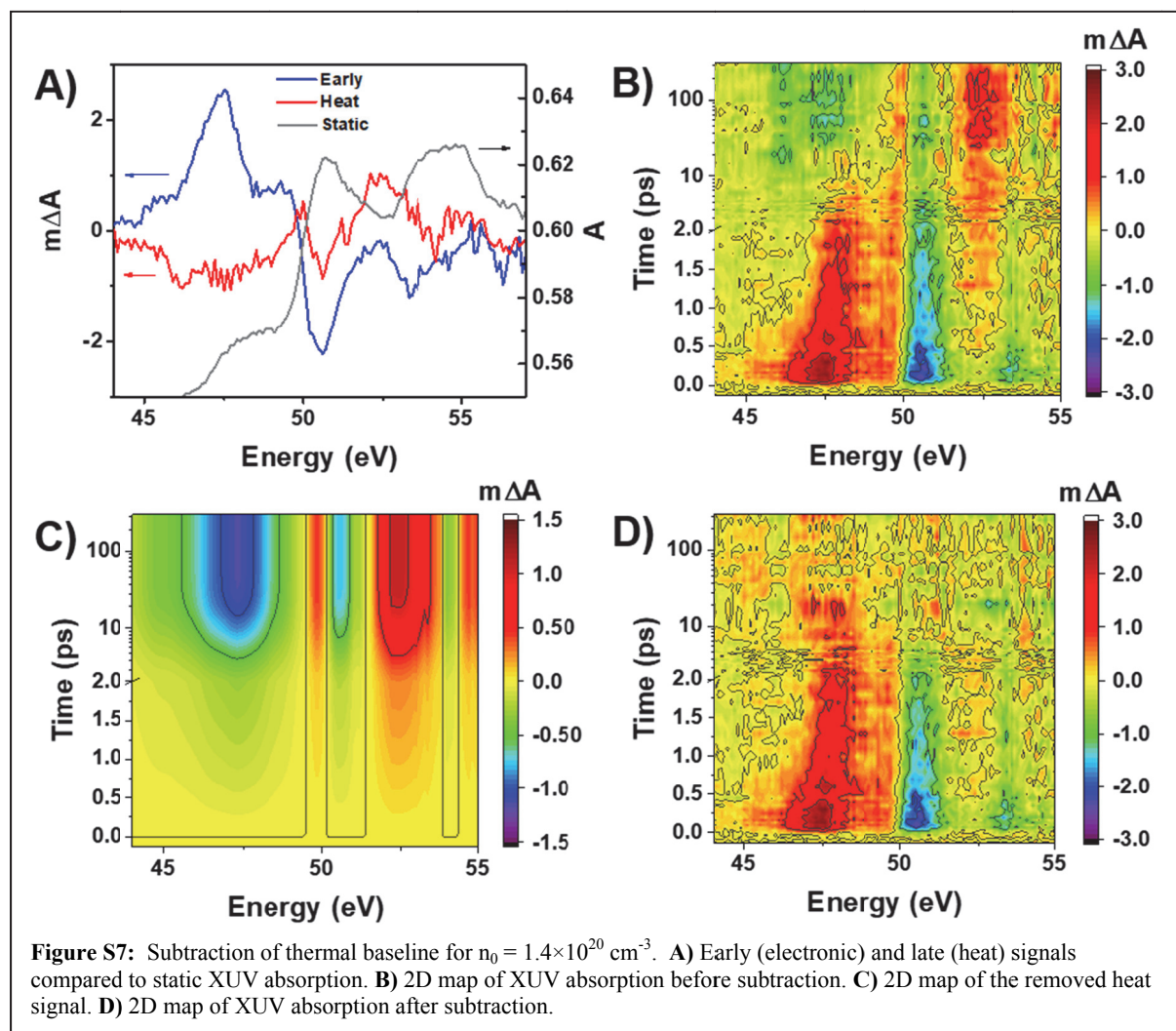
$$A = \sigma \times n \times t$$

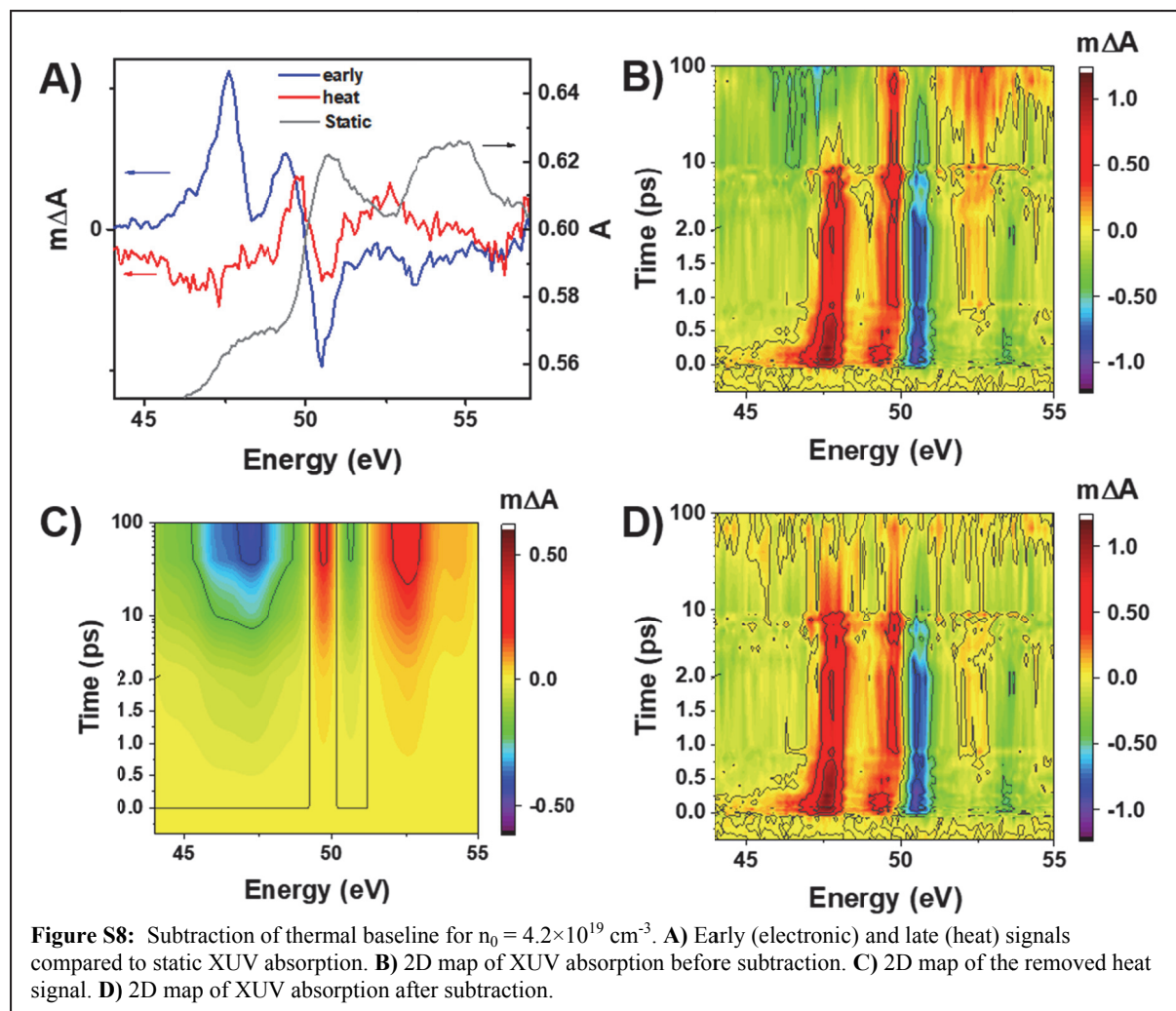
Where A is the integrated extreme ultraviolet absorption in the valence band region, t is the sample thickness, σ is the cross-section, and n is the carrier density. The best fit value gives $\sigma = 1.2 \times 10^{-17} \text{ cm}^2 = 12 \text{ Mbarn}$. This is in agreement with the DFT predicted value (see section on DFT calculations) of 16 Mbarn. Cross-sections are given for \ln absorption. The shown data in Figure S6 is in \log_{10} .



6. Heat Baseline Correction

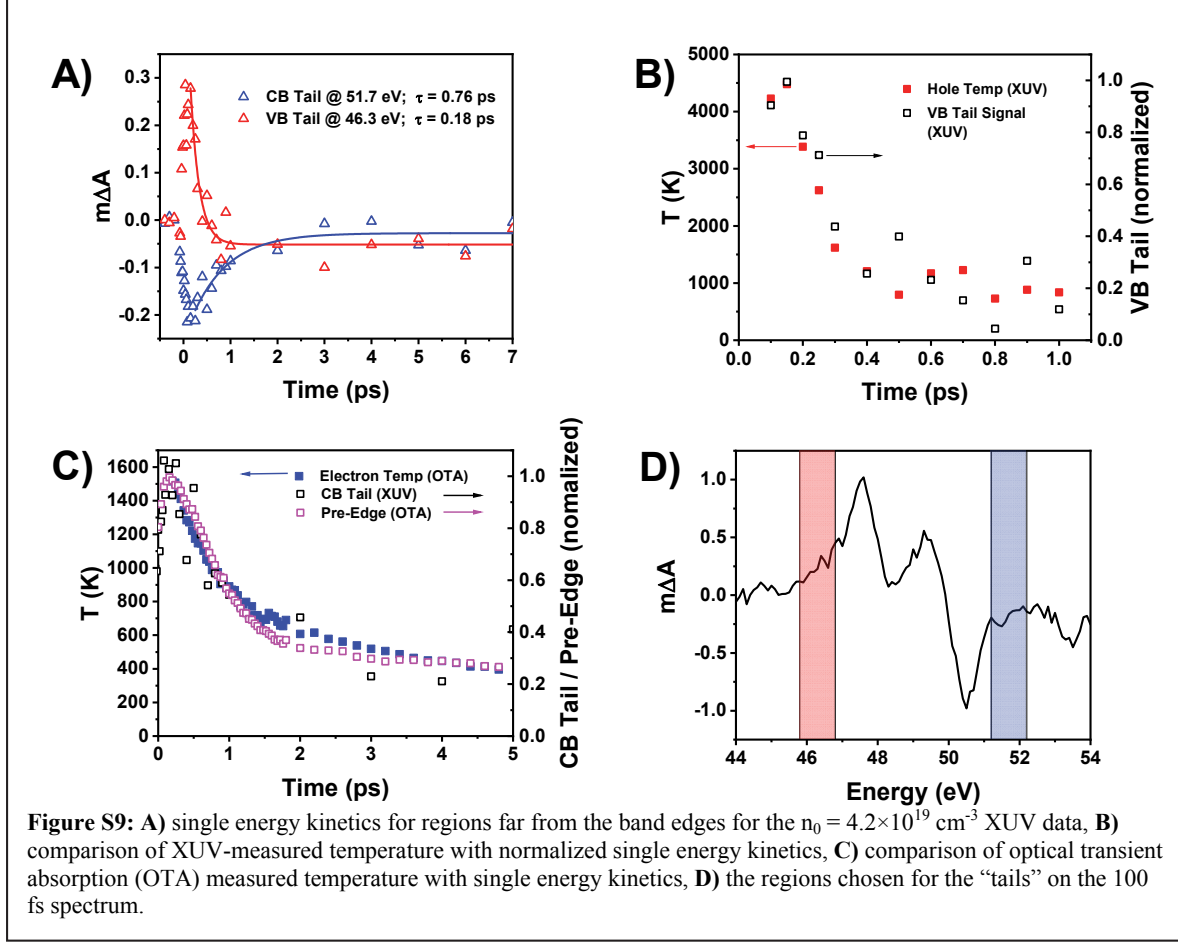
The majority of the energy imparted to the sample by the pump laser is converted into heat. This is visible in the extreme ultraviolet spectrum as a signal that rises on the picosecond timescale. Prior work on lead iodide² has confirmed this by comparing the long-time signal with the difference between a heated sample and a room temperature sample. Global analysis was used to identify the long-time component and its associated rise time. These were used to subtract out the heat component in the data before other interpretation and fitting, shown below in Figure S7 and Figure S8. The time constants identified for the slow rise were 6.9 ps and 11.7 ps for the $1.4 \times 10^{20} \text{ cm}^{-3}$ and $4.2 \times 10^{19} \text{ cm}^{-3}$ initial carrier density data sets, respectively.





7. Single Energy Kinetics

The carrier temperatures over time were compared to single energy kinetics in the data to confirm our interpretation using the $n_0 = 4.2 \times 10^{19} \text{ cm}^{-3}$ data, shown below in Figure S9. For the optical data, the excited state absorption feature below the band gap ($\sim 1.55 \text{ eV}$) is a measure for carrier cooling and its decay matches well with the optically fit carrier temperature decay. For the extreme ultraviolet data, the “tail” of the valence band and conduction band features were examined. A 1 eV averaged region in the valence band tail was shown to have similar kinetics to the extreme ultraviolet fit carrier temperature. A comparable 1 eV averaged region in the conduction band tail was shown to have similar kinetics to the optically fit carrier temperature. The “tail” features were offset such that the long-time value was zero and normalized so that the initial value is 1 to compare to the Fermi temperature kinetics. The shapes of the single energy kinetics and the temperature decays are superimposable, supporting the interpretation of the timing for the processes involved.



8. Optical Transient Absorption Fitting Details

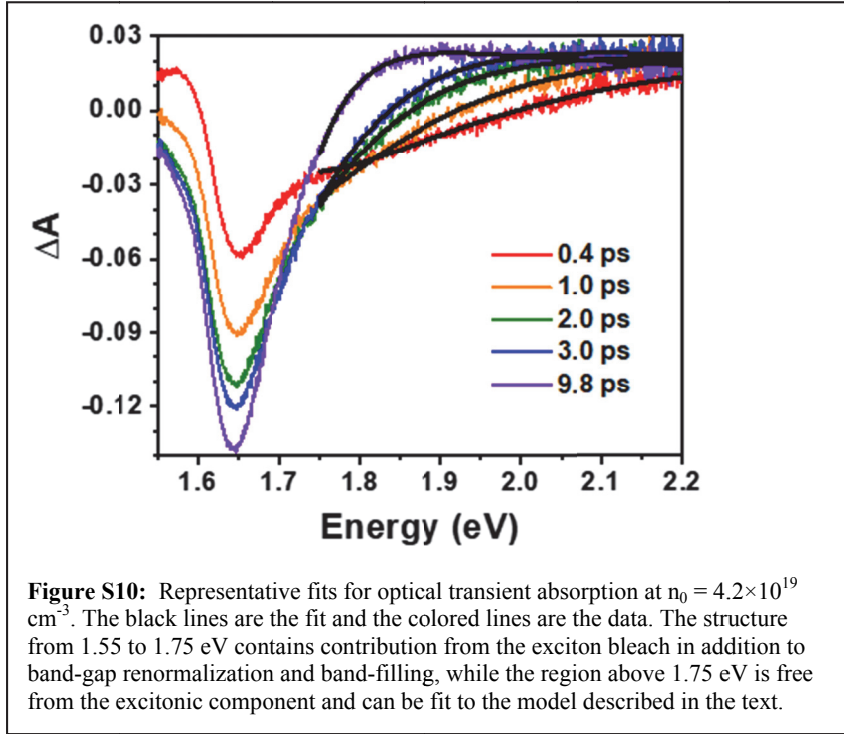
Optical transient absorption data was measured in transmission mode and neglects contributions from changes in the refractive index.³ The transient spectra have contributions from band-filling and bandgap renormalization. Following the approach of Yang et al.⁴, the band-filling component was fit using a Boltzmann distribution applied to a parabolic band model. The bandgap renormalization was fit to the expected $E^{-1/2}$ dependence.

$$\Delta A(E, n) = \frac{A_1}{E} \sqrt{E - E_g(n)} \times \exp\left(-\frac{E - E_f}{2k_B T_c}\right) + A_2 \times \frac{1}{\sqrt{E - E_g(n)}}$$

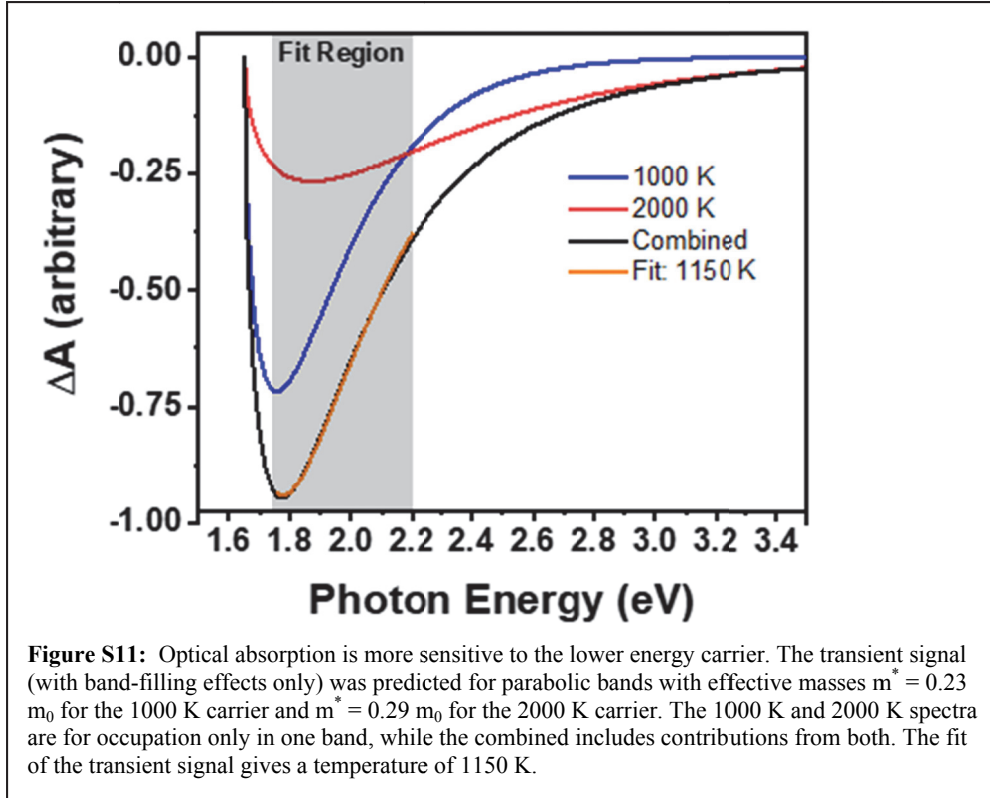
ΔA is the pump-induced change in absorption as a function of energy (E) and carrier concentration (n). A_1 and A_2 are the amplitudes of the band-filling and band gap renormalization components, E_f is the electron quasi-Fermi level, k_B is the Boltzmann constant, T_c is the carrier Fermi temperature, and E_g is the band-gap energy. The fit solves for A_1 , A_2 , and T_c . E_f is approximated as $E_g(n)$ and changes to E_f are accounted for in A_1 . The factor of two in the Boltzmann factor arises from the nearly equal effective masses in perovskite. The band-gap dependence on the carrier density due to band-gap renormalization was approximated using a $n^{1/3}$ dependence with a scale parameter ($\gamma = 1.2 \times 10^{-8} \text{ eV} \cdot \text{cm}$) from the literature.¹

$$\Delta E_{g,BGR}(n) = -2 \times \gamma \times n^{1/3}$$

$\Delta E_{g,BGR}$ is the change in the band-gap energy due to band-gap renormalization and γ is the material dependent scaling parameter. Representative fits are shown in Figure S10. Data was fit over the range of 1.75-2.2 eV to avoid excitonic effects near the band edge.



In semiconductors such as $\text{CH}_3\text{NH}_3\text{PbI}_3$ in which holes and electrons have nearly equal effective masses, optical transient absorption is sensitive to the combined energy distribution of both carriers. However, if the temperatures of electrons and holes are a factor of 1.5 or greater different from each other the fit will be more sensitive to the colder carrier. Figure S11 shows the contributions to the transient spectrum for one carrier at 1000K, the other carrier at 2000K, and the sum of the two spectra. Because in practice the spectrum can only be fit in a narrow energy range due to the presence of higher-energy absorption features above ~ 2.2 eV, the fit preferentially measures the steep slope of the 1000K carrier. For this combination of temperatures, the fit gives a temperature of 1150K. When the two carrier temperatures are within a factor of 1.5 of each other, the fit gives the average temperature.



9. XUV Fitting Details

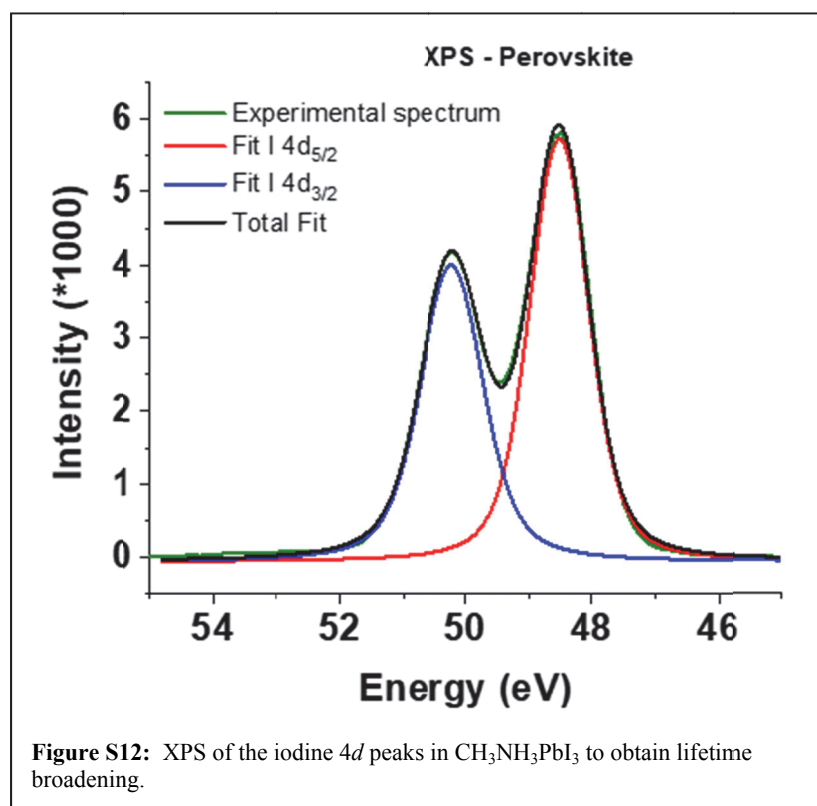
Extreme ultraviolet data was fit using a Fermi function over a parabolic density of states to obtain the characteristic Fermi temperature of the holes in the valence band.

$$\Delta A(E) = k \times \sqrt{E_0 - E} \times \frac{1}{1 + \exp\left(\frac{E_f - E}{k_B T_h}\right)}$$

ΔA is the pump-induced change in absorption in the valence band as a function of energy (E). k is a scaling parameter that represents the curvature of the bands, which was chosen as 0.005 in units of Absorbance to match the rise of the conduction band feature in the ground state absorption (the effective masses of holes and electrons in perovskite are similar). The impact of the chosen value for k is negligible on the resulting values of T_h from the fit. E_0 is the energy difference between the valence band maximum and the core I 4d states. E_f is the quasi Fermi level for the holes in the valence band (as measured from the core I 4d states). k_B is the Boltzmann constant and T_h is the hole Fermi temperature. The fit solves for E_0 , E_f , T_h , and an added offset to account for baseline drift. The above expression was convolved with a Voigt lineshape to represent lifetime (Lorentzian, FWHM = 0.45 eV) and instrumental (Gaussian, FWHM = 0.5 eV) broadening during the fitting process. Fitting to a Boltzmann function instead of a Fermi function gave nearly identical results.

10. I 4d XPS to Identify the Lifetime Broadening

Lifetime broadening was determined using x-ray photoelectron spectroscopy (XPS) of a $\text{CH}_3\text{NH}_3\text{PbI}_3$ sample on a gold-coated silicon wafer, shown in Figure S12 below. XPS was performed on a Kratos Axis ULTRA instrument with a monochromatic aluminum $K\alpha$ x-ray source (1486.61 eV) and a hybrid spherical capacitor energy analyzer. Spectra were collected with an analyzer pass energy of 10 eV. Binding energy scales were calibrated by referencing the gold 4f XPS peak at 84.0 eV. The instrumental (Gaussian) resolution was determined to be 0.38 eV by fitting the gold 4f feature with the Lorentzian width constrained to 0.25 eV. The determined Lorentzian widths for the iodine 4d XPS peaks for $\text{CH}_3\text{NH}_3\text{PbI}_3$ were 0.38 and 0.49 eV. This resulted in the use of the 0.45 eV Lorentzian FWHM for the Voigt lineshape for the extreme-ultraviolet data fitting.



11. Temperature vs Time Fitting Details

The process for energy dissipation from hot carriers has several steps.⁵ Carriers first scatter with longitudinal optical (LO) phonons, then LO phonons decay to form daughter phonons, then the daughter phonon decay to randomize the energy as lattice heat. If the heat capacity of the carrier plasma is sufficiently lower than the heat capacity of the LO phonon modes that they couple to, then the simple Fröhlich model where the LO phonon modes are treated as a bath is applicable. Once the heat capacity of the carrier plasma increases sufficiently (due to more carriers being excited), this model is no longer valid and the hot-phonon bottleneck is present.

The first step for modeling is a single bottleneck, where the carriers and LO phonons rapidly equilibrate and the shared temperature decays as the LO phonon population decays (the transfer between the plasma and the LO is fast compared to the decay of the LO). For sufficiently high occupation (high temperature), the occupation is directly proportional to the temperature and the decay of the temperature in the mode follows first order kinetics. Additionally, when there is sufficiently high carrier density that the recombination is Auger dominated, the Auger recombination adds heat back to the carrier plasma.

$$\frac{dT_{LO}}{dt} = -\frac{T_{LO} - T_L}{\tau_{LO}} + \frac{2}{3k_B} \times E_g \times \chi_{e,h} \times k_3 \times n^2$$

T_{LO} is the temperature of the LO phonon distribution (and thus the carriers due to the bottleneck). T_L is the temperature of the lattice. t is time. τ_{LO} is the LO phonon lifetime. k_B is the Boltzmann constant, E_g is the band-gap, k_3 is the third order recombination rate constant, and $n(t)$ is the time-dependent carrier density. $\chi_{e,h}$ is the Auger branching ratio. The $2/(3k_B)$ term for the Auger derives from the heat capacity of the carrier plasma. This model fails to fit the data for both data sets ($n_0 = 1.4 \times 10^{20} \text{ cm}^{-3}$ and $4.2 \times 10^{19} \text{ cm}^{-3}$) because a second bottleneck (for the equilibrium between the LO mode and its daughter phonons) is present. The temperature is thus fit using coupled equations for the LO and daughter temperatures (the rate of transfer between the modes and decay of the daughter are comparable), below.

$$\begin{aligned} \frac{dT_{LO}}{dt} &= \frac{-(T_{LO} - T_A)}{\tau_{LO}} + \frac{2}{3k_B} \times E_g \times \chi_{e,h} \times k_3 \times n^2 \\ \frac{dT_A}{dt} &= \frac{c_{LO} \times (T_{LO} - T_A)}{c_A \times \tau_{LO}} - \frac{(T_A - T_L)}{\tau_A} \end{aligned}$$

T_A is the temperature of the acoustic (daughter) phonons. τ_A is the decay constant for the acoustic phonons. c_{LO} and c_A are the heat capacities of the LO and daughter phonons respectively. In this model, the adjustable fit parameters are the initial temperature (T_0), the LO lifetime, the acoustic lifetime, and the ratio of heat capacities (c_{LO} / c_A). These values are shown in Table 1. The LO lifetimes are comparable to the value of ~ 0.6 ps reported in the literature,⁶ as are the acoustic lifetimes⁷ of ~ 4 ps. The deviation in lifetimes between the two initial fluences are likely due to the larger presence of Auger in the higher fluence data set. If the Auger branching ratio is uneven, then that will alter the kinetics in the fit. This branching ratio has not been measured, so values for equal ($\chi_h = 0.5$) and completely electron-hole-hole dominated ($\chi_h = 1$) were used in the

fit as reasonable bounds for the data. The values reported for the time constants in the main paper are the averages of the two extremes for each data set.

Table 1: Double bottleneck fit parameters for OTA data

n_0 (cm ⁻³)	χ_h	T_0 (K)	τ_{LO}	τ_A	c_{LO}/c_A
1.4×10^{20}	0.5	2100 ± 100	0.2 ± 0.1	3.6 ± 0.3	0.1 ± 0.1
4.2×10^{19}	0.5	1900 ± 100	0.6 ± 0.1	1.0 ± 0.3	0.1 ± 0.1
1.4×10^{20}	1	2400 ± 100	0.9 ± 0.1	4.6 ± 0.3	0.8 ± 0.1
4.2×10^{19}	1	1900 ± 100	1.0 ± 0.1	5.8 ± 0.3	0.4 ± 0.1

Using the same two-bottleneck model for the 1.4×10^{20} cm⁻³ XUV data gives the results present in Table 2. This was fit for the first 3 ps as the signal-to-noise ratio was not sufficient for later time data due to the fast recombination at this excitation density. This is responsible for the large error in the acoustic lifetime.

Table 2: Double bottleneck fit parameters for XUV data

n_0 (cm ⁻³)	χ_h	T_0 (K)	τ_{LO}	τ_A	c_{LO}/c_A
1.4×10^{20}	0.5	7000 ± 600	0.5 ± 0.1	13 ± 70	0.2 ± 0.1
1.4×10^{20}	1	7300 ± 600	0.4 ± 0.1	14 ± 70	0.1 ± 0.1

The XUV data at 4.2×10^{19} cm⁻³ is fit for the first 400 fs using the below-bottleneck Fröhlich model. In this model (equation below), there are two constraints and two fit parameters.

$$\frac{dT_h}{dt} = -\frac{2}{3k_B} \frac{\hbar\omega_{LO}}{\tau_{h-LO}} \left[\exp\left(\frac{-\hbar\omega_{LO}}{k_B T_h}\right) - \exp\left(\frac{-\hbar\omega_{LO}}{k_B T_L}\right) \right]$$

T_h and T_L are the hole temperature and the lattice temperature (this assumes that the LO phonon distribution has sufficiently high heat capacity to remain at the lattice temperature). T_L is set at 300 K for this model. \hbar is the reduced Planck constant, ω_{LO} is the LO phonon (angular) frequency, and τ_{h-LO} is the characteristic scattering time between the holes and the phonons. In the main paper, $\hbar\omega_{LO}$ is set to 29 meV, but for completeness we include the 14 meV phonon fit here. The fit parameters are T_0 (initial hole temperature) and τ_{h-LO} , with results shown in Table 3.

Table 3: Fröhlich model parameters for XUV data

n_0 (cm ⁻³)	$\hbar\omega_{LO}$ (meV)	T_0 (K)	τ_{h-LO} (fs)
4.2×10^{19}	29	6000 ± 1000	8.0 ± 2.7
4.2×10^{19}	14	6000 ± 1000	2.3 ± 0.8

This fit time constant may be compared to the results for the interaction of a charge and a dipole in a polar semiconductor.⁸

$$\frac{1}{\tau_{e/h-LO}} = \frac{e^2}{2\pi\hbar} \left(\frac{\omega_{LO} m^*}{2\hbar} \right)^{1/2} \left(\frac{1}{\mathcal{E}_\infty} - \frac{1}{\mathcal{E}_s} \right)$$

The rate constant can be estimated if the phonon frequency (ω_{LO}), effective mass (m^*), and static (\mathcal{E}_s) and optical (\mathcal{E}_∞) dielectric constants are known. An effective mass of $0.29 m_0$ was used.⁹ A

range of dielectric constants have been computationally predicted and measured for $\text{CH}_3\text{NH}_3\text{PbI}_3$.¹⁰ From the range of experimental values, the time constant was calculated using the smallest difference (low static, 13, and high optical, 6.5) and greatest difference (high static, 36.9, and low optical, 4). The average value of these two calculations gives an estimate of 8.5 fs for the 29 meV phonon, a good match to the fit value in Table 4. The same process was performed for the 14 meV phonon, resulting in 12.5 fs. This prediction differs by a factor of five from the 2.3 fs fit value in Table 3. The excellent match between the measured and predicted scattering times for the 29 meV phonon gives additional support to the computationally-predicted claim that holes scatter preferentially with hot phonons,¹¹ but experiments at lower pump fluence will be required to confirm this tentative assignment.

12. Computational Details

Density functional theory (DFT) calculations are performed using the VASP software.^{12,13} The projector augmented wave (PAW) scheme is used to describe electron-ion interaction and semi-core I_{4d} states are described as valence electrons. Exchange and correlation is calculated using the generalized-gradient approximation (GGA) by Perdew, Burke, and Ernzerhof (PBE).¹⁴ Spin-orbit coupling is included in the calculation of electronic structure and optical response.¹⁵ A plane-wave cutoff energy of 750 eV is chosen to converge to total cell energy per atom below a threshold of 5 meV per atom. A $7 \times 7 \times 7$ randomly shifted \mathbf{k} -point mesh is used for computing optical spectra using the DFT level of theory. Linear optical response is calculated by the Ehrenreich-Cohen formula for the temperature and frequency-dependent dielectric tensor $\epsilon^{\alpha\beta}(\omega)$.¹⁶ The imaginary component is given by:

$$\epsilon_2^{\alpha\beta}(\omega) = \frac{8\pi^2 e^2}{\Omega} \sum_{n'n\mathbf{k}} f_{n\mathbf{k}}^{qf} (1 - f_{n'\mathbf{k}}^{qf}) \frac{\langle \phi_{n'\mathbf{k}} | \hat{p}_\alpha | \phi_{n\mathbf{k}} \rangle \langle \phi_{n\mathbf{k}} | \hat{p}_\beta | \phi_{n'\mathbf{k}} \rangle}{(\epsilon_{n'\mathbf{k}} - \epsilon_{n\mathbf{k}})^2} \delta(\epsilon_{n'\mathbf{k}} - \epsilon_{n\mathbf{k}} - \hbar\omega)$$

Where $\phi_{n\mathbf{k}}$ and $\epsilon_{n\mathbf{k}}$ are the Kohn-Sham eigen-states and energies at band n and wave vector \mathbf{k} . Ω is the cell volume and \hat{p}_α is the momentum operator in the α Cartesian direction. $f_{n\mathbf{k}}$ and $(1 - f_{n'\mathbf{k}})$ are the quasi-Fermi distributions of an electronic state at band index n and wave vector \mathbf{k} being occupied and a state at n' and \mathbf{k} being empty. For core-to-conduction band transitions n' is a conduction band index and n is a core band index. For core-to-valence band transitions of semi-core-hole excitations, n' is a partially filled valence band and n is a core band. The XUV cross section of holes was computed by integrating over the absorption coefficient of the transition from $I 4d_{5/2}$ to a partially filled valence band, where the hole distribution was defined by a Fermi function. The position of the quasi-Fermi hole energy of the excited holes is determined by solving the integral equation:

$$n_h = \int_{-\infty}^{\infty} \rho_{VB}(E) f^{qf}(E, E_{qfh}, T_h) dE$$

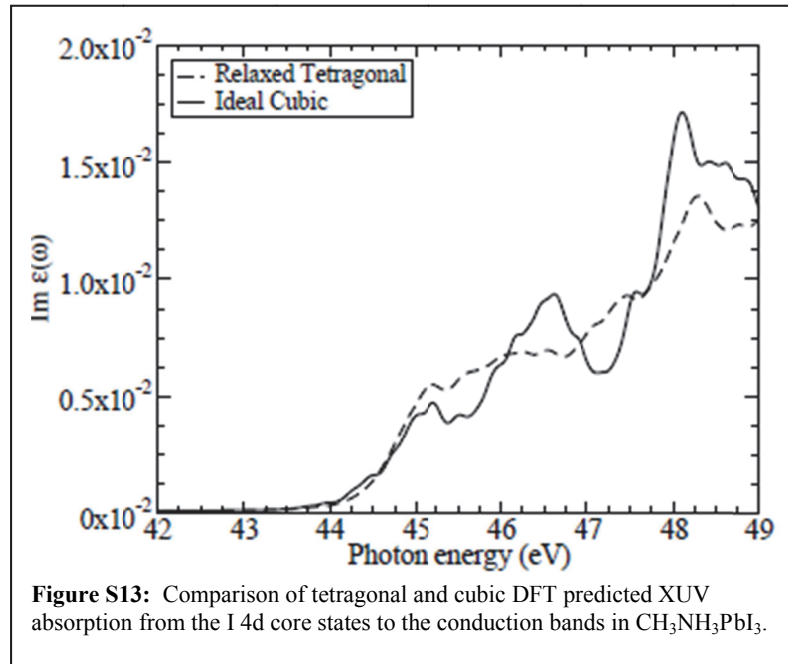
Here, $\rho_{VB}(E)$ is the density of states of the valence states, f^{qf} is the quasi-Fermi distribution of the excited holes, E_{qfh} is the quasi-Fermi energy of the excited holes, and T_h is the Fermi-

temperature of the holes. The density of excited holes n_h and Fermi-temperature of the holes T_h are chosen from experimentally measured values.

The effect of exciton formation on the dielectric function is included by solving the Bethe-Salpeter equation (BSE) for the optical polarization function. The BSE is reformulated as an eigenvalue problem where the eigenvalues E^A are the two-particle excitation energy. The corresponding excitonic Hamiltonian is:^{17,18}

$$H_{cvk}^{c'v'k'} = (\epsilon_{ck} - \epsilon_{vk})\delta_{cc'}\delta_{vv'}\delta_{kk'} - W_{cvk}^{c'v'k'} + 2\bar{V}_{cvk}^{c'v'k'}$$

Here, W and \bar{V} are the statically screened Coulomb interaction and unscreened exchange interaction between electrons excited to the conduction bands and holes excited to the valence bands. The diagonal components include band energy differences between conduction and valence states. The imaginary dielectric function is calculated by a time-propagation technique.^{19,20} 55926 time steps of ≈ 0.00894 per eV are required to calculate a spectrum up to excitation energies of 50 eV. Due to the high computational demand of including 50 eV of transitions in the optical spectrum with excitonic contributions, the simpler perfect cubic phase is simulated and a randomly shifted $5 \times 5 \times 5$ k-point mesh is used to sample the Brillouin zone. The ground state spectra without excitons of the perfect cubic phase and relaxed tetragonal phase are very similar, as shown in Figure S13. The input dielectric constant in the statically screened Coulomb interaction is varied between $\epsilon_r = 1$ to $\epsilon_r = 6$ to determine the best theoretical prediction of experimental results for core-hole excitonic effects. A dielectric constant of $\epsilon_r = 1.5$ best predicts the exciton peaks observed in the ground state experimental spectra. High energy excitations from the semi-core states are generally localized and thus not heavily screened. As such, the choice of $\epsilon_r = 1.5$ is justified for an approximate approach. A fuller understanding would have to be found via a fully dynamical calculation of the screened Coulomb interaction, which is currently computationally intractable.



13. References

1. Yang, Y. *et al.* Observation of a hot-phonon bottleneck in lead-iodide perovskites. *Nat. Photonics* **10**, 53–59 (2016).
2. Lin, M.-F. *et al.* Carrier-Specific Femtosecond XUV Transient Absorption of PbI₂ Reveals Ultrafast Nonradiative Recombination. *J. Phys. Chem. C* **121**, 27886–27893 (2017).
3. Price, M. B. *et al.* Hot-carrier cooling and photoinduced refractive index changes in organic–inorganic lead halide perovskites. *Nat. Commun.* **6**, 8420 (2015).
4. Yang, J. *et al.* Acoustic-optical phonon up-conversion and hot-phonon bottleneck in lead-halide perovskites. *Nat. Commun.* **8**, 14120 (2017).
5. Klimov, V., Haring Bolivar, P. & Kurz, H. Hot-phonon effects in femtosecond luminescence spectra of electron-hole plasmas in CdS. *Phys. Rev. B* **52**, 4728–4731 (1995).
6. Fu, J. *et al.* Hot carrier cooling mechanisms in halide perovskites. *Nat. Commun.* **8**, 1300 (2017).
7. Li, B. *et al.* Polar rotor scattering as atomic-level origin of low mobility and thermal conductivity of perovskite CH₃NH₃PbI₃. *Nat. Commun.* **8**, 16086 (2017).
8. Ridley, B. K. Hot phonons in high-field transport. *Semicond. Sci. Technol.* **4**, 1142–1150 (1989).
9. Giorgi, G., Fujisawa, J. I., Segawa, H. & Yamashita, K. Small photocarrier effective masses featuring ambipolar transport in methylammonium lead iodide perovskite: A density functional analysis. *J. Phys. Chem. Lett.* **4**, 4213–4216 (2013).
10. Wilson, J. N., Frost, J. M., Wallace, S. K. & Walsh, A. Dielectric and ferroic properties of metal halide perovskites Dielectric and ferroic properties of metal halide perovskites. *APL Mater.* **7**, 010901 (2019).
11. Li, W., Zhou, L., Prezhd, O. V. & Akimov, A. V. Spin–Orbit Interactions Greatly Accelerate Nonradiative Dynamics in Lead Halide Perovskites. *ACS Energy Lett.* **3**, 2159–2166 (2018).
12. Kresse, G. & Furthmüller, J. Efficient iterative schemes for ab initio total-energy calculations using a plane-wave basis set. *Phys. Rev. B* **54**, 11169–11186 (1996).
13. Kresse, G. & Joubert, D. From ultrasoft pseudopotentials to the projector augmented-wave method. *Phys. Rev. B* **59**, 1758–1775 (1999).
14. Perdew, J. P., Burke, K. & Ernzerhof, M. Generalized Gradient Approximation Made Simple. *Phys. Rev. Lett.* **77**, 3865–3868 (1996).
15. Steiner, S., Khmelevskiy, S., Marsmann, M. & Kresse, G. Calculation of the magnetic anisotropy with projected-augmented-wave methodology and the case study of disordered Fe_{1-x}Co_x alloys. *Phys. Rev. B* **93**, 224425 (2016).
16. Ehrenreich, H. & Cohen, M. H. Self-Consistent Field Approach to the Many-Electron Problem. *Phys. Rev.* **115**, 786–790 (1959).
17. King, P. D. C. *et al.* Determination of the branch-point energy of InN: Chemical trends in common-cation and common-anion semiconductors. *Phys. Rev. B* **77**, 45316 (2008).
18. Onida, G., Reining, L. & Rubio, A. Electronic excitations: density-functional versus many-body {Green}'s-function approaches. *Rev. Mod. Phys.* **74**, 601–659 (2002).
19. Hahn, P. H., Schmidt, W. G. & Bechstedt, F. Bulk Excitonic Effects in Surface Optical Spectra. *Phys. Rev. Lett.* **88**, 16402 (2001).

20. Schmidt, W. G., Glusch, S., Hahn, P. H. & Bechstedt, F. Efficient $O(N^2)$ method to solve the Bethe-Salpeter equation. *Phys. Rev. B* **67**, 085307 (2003).